Hindawi
Shock and Vibration
Volume 2023, Article ID 5577119, 16 pages
https://doi.org/10.1155/2023/5577119

Research Article

Coordination Control of Active Steering and Direct Yaw Control for the Articulated Steering Vehicle

Bin Huang,[1,2] Zhijun Yuan,[3] Dengzhi Peng,[1,4] Xiaoxu Wei,[1,2] and Yongsheng Wang[5]

[1]*Hubei Key Laboratory of Advanced Technology for Automotive Components, Wuhan University of Technology, Wuhan 430070, China*
[2]*School of Automotive Engineering, Wuhan University of Technology, Wuhan 430063, China*
[3]*Guangxi Automobile Group Co. Ltd., Liuzhou 545007, China*
[4]*Dongfeng Off-Road Vehicle Co. Ltd., Shiyan 442013, China*
[5]*School of Information Engineering, Wuhan University of Technology, Wuhan 430070, China*

Correspondence should be addressed to Xiaoxu Wei; wxx2014@whut.edu.cn

Received 21 March 2023; Revised 8 May 2023; Accepted 10 May 2023; Published 9 June 2023

Academic Editor: Xiuquan Liu

Lateral stability is vital to vehicle handling stability and traffic safety. It is also a crucial factor for the path-tracking ability of the vehicle in the intelligent transportation system (ITS). Most of the research focuses on vehicles with an Ackerman steering system. The ASV (articulated steering vehicle) has a lower steering radius. Thus, it is widely used in some special vehicles, such as mining and construction vehicles. The ASV has weaker lateral stability than the vehicle with an Ackerman steering system. To improve the stability of an ASV, the nonlinear lateral dynamic model is established and validated by field test. With the lateral dynamic model, the steering characteristic of the ASV is analyzed. Based on the stability criteria analysis, the vehicle sideslip angle and angular velocity phase portrait are chosen as the stability indicator. An integrated AASS (active articulated steering system) DYC (direct yaw control) controller based on the adaptive MPC (model predictive control) method is designed according to the track on the phase plane. The double lane-change and 0.7 Hz sine with dwell maneuver are initiated based on the integrated vehicle dynamic model. The results suggest that the provided controller has a better stability performance than the current antiwindup PID control algorithm. It lays a good foundation for the vehicle safety and path tracking of ASV in the ITS.

1. Introduction

ASV (articulated steering vehicle) is a vehicle with an articulated steering system. Normally, the front and rear parts of the ASV form an angle to allow the vehicle to change its direction as the driver's intention. It is widely used in the engineering area, such as loaders and mining vehicles. Developing the intelligent transportation system (ITS) for these vehicles to ease the burden of the driver or liberate them from crucial work conditions is necessary and meaningful. Without the participation of the pedestrian and with the enclosed working condition, the scenario of these ASV in an intelligent transportation system is simpler than the passenger cars. However, the dynamic characteristics of the ASV are quite different from the vehicle with the Ackerman steering system due to its unique mechanical structure. The advantage of an ASV is that it has a lower radius during the steering process [1]. The weakness of the ASV is that it has relatively weaker lateral stability compared to the vehicle with the Ackerman steering system [2].

Plenty of work has been carried out to strengthen the vehicle's lateral stability, most of them focusing on the vehicle with an Ackerman steering system. Jin et al. provide an integrated AFS (active front steering) and ASS (active suspension system) controller to improve the vehicle handling stability based on a gain-scheduling state-feedback controller [3]. A full X-by-wire chassis coordinated control scheme utilizing the AFS, DYC (direct yaw control), ARC, and ASR is provided to improve the vehicle's longitudinal, yaw, and roll stability synthetically [4]. Aouadj et al.

set up a controller to coordinate AFS and DYC based on sliding mode. The AFS and DYC system is designed based on the phase plane portrait [5]. The robust Takagi–Sugeno fuzzy control is initiated to combine the AFS and DYC systems [6]. Besides, MPC (model predictive control) [7] and NMPC (nonlinear model predictive control) [8] are also applied in this area. The good lateral stability also lays a good foundation for the autonomous driving vehicle [9]. The vehicle with the distribution driving system equipped with lots of sensors, the influence of poor SNR (signal-to-noise ratio), and the fault of the sensor are also analyzed and handled by the researchers [10, 11].

For the ASV, the current research focuses on the effect of the hydraulic steering system on the vehicle dynamics [12, 13], lateral stability influence factor analysis [14], improving the vehicle stability by the control of ASS [15], and antirollover system [16].

A typical architecture of the controller for vehicle stability control is shown in Figure 1. The reference model is a 2 or 3 DOFs (degree of freedoms) that provides the ideal yaw rate and vehicle sideslip angle of the vehicle [17]. Normally, the multilayer controller is used. The upper controller estimates the vehicle state and generates the active steering angle and torque, and the lower controller distributes the torque to the motors. Gao et al. provide a vehicle-based method to estimate the attitude of underground ASV [18]. For the torque distribution algorithms, generalized inversion [19] and quadratic programming methods [20] are provided. The active steering angle and torque are sent to a vehicle dynamic model with 8, 10, or 14 DOFs to verify the effect of the controller.

To improve the lateral stability of an ASV, the AASS (active articulated steering system) is combined with the DYC system. The reference model with 2 DOFs and an integrated simulation vehicle model is built and verified by the field test result. Based on the nonlinear reference model, the boundary of the ideal yaw rate and vehicle sideslip angle is determined. The integrated controller is designed based on the vehicle stability status judged by the vehicle sideslip angle and sideslip angular velocity phase portrait. The torque of the driving system and active articulated angle is coordinated by the MPC method. The provided controller is verified by comparing the vehicle performance to the reference model, without control, and with a current anti-windup PID controller.

2. Vehicle Lateral Dynamic Model

For the lateral dynamics control of the vehicle, it is not common to use a complex vehicle and dynamic model. Normally, a simplified lateral dynamic model with 2 DOFs is used to design and implement the controller [21]. A typical 2 DOFs model is shown in Figure 2. Since this model mainly focuses on the lateral dynamic features, other motions, such as roll, pitch, and vertical, are neglected. Due to its unique mechanic structure, the lateral and yaw motion of the ASV can be described by equations (1) and (2), respectively.

$$m_f \dot{v}_{\mathrm{yf}} + m_r \dot{v}_{\mathrm{yr}} = F_{\mathrm{yfl}} + F_{\mathrm{yrl}} + F_{\mathrm{yfr}} + F_{\mathrm{yrr}}, \tag{1}$$

$$\left[I_f + I_r + m_r\left(L_{f2} + L_{r2}\right)^2\right]\dot{\omega} = L_{f1}\left(F_{\mathrm{yfl}} + F_{\mathrm{yfr}}\right) - L_{\mathrm{rf}}\left(F_{\mathrm{yrl}} + F_{\mathrm{yrr}}\right) + m_r \dot{v}_{\mathrm{yr}}\left(L_{r2} + L_{f2}\right) + \Delta M. \tag{2}$$

In equations (1) and (2), m_i means the mass, v_{yi} represents the lateral velocity, F_{yij} is the tire force, I_i means the yaw moment of the inertia, the footnote $i = f, r$ means the front and rear vehicle body, $j = l, r$ represents the left and right side of the vehicle, L_{i1} and L_{i2} are the distance between the CG (center of gravity) to the axle and articulation point, ω is the vehicle yaw rate, L_w is the wheelbase, and ΔM means the external yaw moment. The detail of the annotation in this paper is listed in the abbreviations. The relationship between the lateral velocity and longitudinal velocity can be established by the following equation:

$$\begin{cases} \dot{v}_{\mathrm{yf}} = v_{\mathrm{xf}}\dot{\beta} + v_{\mathrm{xf}}\omega, \\ \dot{v}_{\mathrm{yr}} = v_{\mathrm{xf}}\dot{\beta} - \left(L_{f2} + L_{r2}\right)\dot{\omega} + v_{\mathrm{xf}}\omega, \end{cases} \tag{3}$$

where β is the vehicle sideslip angle. The relationship between the lateral force and tire sideslip angle is nonlinear. Therefore, a nonlinear tire model is necessary to calculate the lateral force. A brush tire model variant of the Fiala nonlinear brush model is used in this model. It assumes one coefficient of friction and parabolic force distribution [22]. In the brush model, the lateral force, F_{yi}, can be expressed as follows:

$$F_{\mathrm{yi}} = \frac{C_{\alpha i} f\left(\xi_i\right) \tan \alpha_i}{\xi_i \left(1 + \lambda_i\right)}, \tag{4}$$

$$f\left(\xi_i\right) = \begin{cases} \xi_i - \dfrac{\xi_i^2}{3\mu F_{\mathrm{zi}}} + \dfrac{\xi_i^3}{27\mu^2 F_{\mathrm{zi}}^2}, & \left|\xi_i\right| < 3\mu F_{\mathrm{zi}}, \\ \mu F_{\mathrm{zi}}, & \left|\xi_i\right| \geq 3\mu F_{\mathrm{zi}}, \end{cases} \tag{5}$$

$$\xi_i = \sqrt{C_{\mathrm{xi}}^2\left(\frac{\lambda_i}{1 + \lambda_i}\right)^2 + C_{\alpha i}^2\left(\frac{\tan \alpha_i}{1 + \lambda_i}\right)^2}, \tag{6}$$

$$\lambda_i = \frac{R_\omega \omega_i - v_{\mathrm{xf}}}{\max\left(R_\omega \omega_i, v_{\mathrm{xf}}\right)}, \tag{7}$$

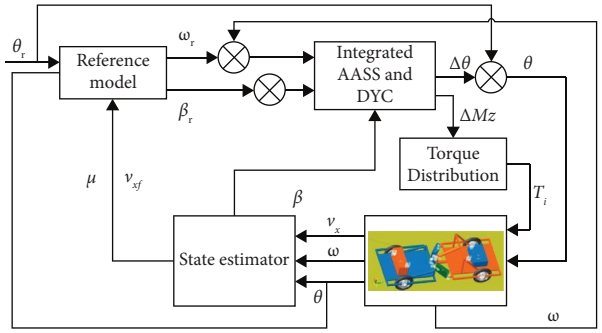

Figure 1: Architecture of vehicle controller.

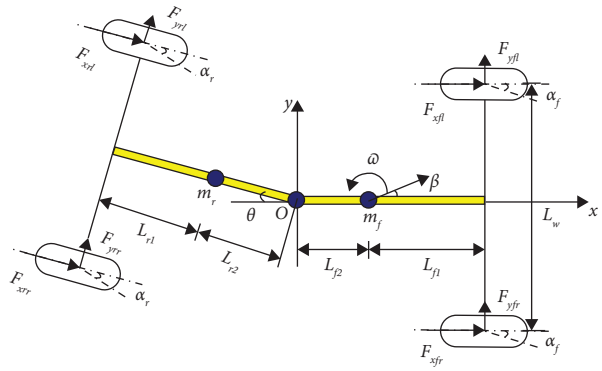

Figure 2: Vehicle lateral dynamic model.

where λ_i is the slip rate of the wheel, μ represents the road adhesion coefficient, and C_{xi} and $C_{\alpha i}$ are the longitudinal and lateral stiffness of the tire. The tire sideslip angle, α_i, can be gained by the following equation:

$$\begin{cases} \alpha_f = \beta + \dfrac{L_{f1}\omega}{v_{xf}}, \\ \alpha_r = \beta - \dfrac{L_{rf}\omega}{v_{xf}} + \theta. \end{cases} \tag{8}$$

Here, θ means the articulation angle. The normal load of the wheels on the front and rear axle, F_{zf} and F_{zr}, can be defined as follows:

$$\begin{cases} F_{\mathrm{zf}} = \dfrac{m_f g\left(L_{r1} + L_{f2} + L_{r2}\right) + m_r g L_{r1}}{2\left(L_{f1} + L_{f2} + L_{r2} + L_{r1}\right)}, \\ F_{\mathrm{zr}} = \dfrac{m_r g\left(L_{f1} + L_{f2} + L_{r2}\right) + m_r g L_{f1}}{2\left(L_{f1} + L_{f2} + L_{r2} + L_{r1}\right)}, \end{cases} \tag{9}$$

where α_{sl} is the sideslip angle that corresponds to the full saturation of the lateral tire force.

$$\alpha_{\mathrm{sl}} = \arctan\frac{3\mu F_z}{C_\alpha}. \tag{10}$$

Based on equations (1)–(10), the state-space representation of the lateral dynamic model can be written as follows:

$$\dot{x}(t) = \mathrm{A}x(t) + B_1 u_1(t) + B_2 u_2(t), \tag{11}$$

where $x(t)$ is the state vector, A is the system matrix, B_1 and B_2 are the control input matrixes, and $u_1(t)$ and $u_2(t)$ are the control input vectors.

$$
\begin{aligned}
x(t) &= [\,\beta \;\; \omega\,]^T,\\
A &= \begin{bmatrix} a_{11} & a_{12} \\ a_{21} & a_{22} \end{bmatrix},\\
B_1 &= \begin{bmatrix} b_{11} \\ b_{21} \end{bmatrix},\\
u_1(t) &= \theta,\\
B_2 &= \begin{bmatrix} b_{12} & b_{13} \\ b_{21} & b_{23} \end{bmatrix},\\
u_2(t) &= [\,\Delta\theta \;\; \Delta M\,]^T,\\
a_{11} &= \frac{\left(K_f(\alpha_f)+K_r(\alpha_r)\right)\left(I_f+I_r+2m_r\left(L_{f2}+L_{r2}\right)^2\right)+m_r\left(L_{f1}K_f(\alpha_f)-L_{rf}K_r(\alpha_r)\right)\left(L_{f2}+L_{r2}\right)}{v_{xf}\left(m_f+m_r\right)\left(I_f+I_r+2m_r\left(L_{f2}+L_{r2}\right)^2\right)-2m_r v_{xf}\left(m_f+m_r\right)\left(L_{f2}+L_{r2}\right)^2},\\
a_{12} &= -\frac{\left(v_{xf}\left(m_f+m_r\right)-(1/v_{\mathrm{xf}})\left(L_{f1}K_f(\alpha_f)-L_{rf}K_r(\alpha_r)\right)\left(I_f+I_r+2m_r\left(L_{f2}+L_{r2}\right)^2\right)\right)\left(L_{f2}+L_{r2}\right)}{v_{xf}\left(m_f+m_r\right)\left(I_f+I_r+2m_r\left(L_{f2}+L_{r2}\right)^2\right)-2m_r v_{\mathrm{xf}}\left(m_f+m_r\right)\left(L_{f2}+L_{r2}\right)^2}\\
&\quad+\frac{(m_r/v_{\mathrm{xf}})\left(L_{f1}^2K_f(\alpha_f)+L_{rf}^2K_r(\alpha_r)\right)-m_r v_{\mathrm{xf}}\left(L_{f2}+L_{r2}\right)^2}{v_{\mathrm{xf}}\left(m_f+m_r\right)\left(I_f+I_r+2m_r\left(L_{f2}+L_{r2}\right)^2\right)-2m_r v_{xf}\left(m_f+m_r\right)\left(L_{f2}+L_{r2}\right)^2},\\
a_{21} &= \frac{\left(m_f+m_r\right)\left(L_{f1}K_f(\alpha_f)-L_{rf}K_r(\alpha_r)\right)+m_r\left(K_f(\alpha_f)+K_r(\alpha_r)\right)\left(L_{f2}+L_{r2}\right)}{\left(m_f+m_r\right)\left(I_f+I_r+2m_r\left(L_{f2}+L_{r2}\right)^2\right)-m_r^2\left(L_{f2}+L_{r2}\right)^2},\\
a_{22} &= \frac{L_{f1}^2K_f(\alpha_f)+L_{rf}^2K_r(\alpha_r)+m_r v_{\mathrm{xf}}^2\left(L_{f2}+L_{r2}\right)\left(m_f+m_r\right)}{v_{xf}\left(m_f+m_r\right)\left(I_f+I_r+2m_r\left(L_{f2}+L_{r2}\right)^2\right)-m_r^2 v_{xf}\left(L_{f2}+L_{r2}\right)^2}\\
&\quad-\frac{m_r\left(v_{xf}^2\left(m_f+m_r\right)-\left(L_{f1}K_f(\alpha_f)-L_{rf}K_r(\alpha_r)\right)\right)\left(L_{f2}+L_{r2}\right)}{v_{xf}\left(m_f+m_r\right)\left(I_f+I_r+2m_r\left(L_{f2}+L_{r2}\right)^2\right)-m_r^2 v_{xf}\left(L_{f2}+L_{r2}\right)^2},\\
b_{11} &= b_{12} = -\frac{K_r(\alpha_r)\left(I_f+I_r+2m_r\left(L_{f2}+L_{r2}\right)^2\right)-L_{rf}K_r(\alpha_r)m_r}{m_r v_{xf}\left(m_f+m_r\right)\left(L_{f2}+L_{r2}\right)+m_r^2 v_{xf}\left(L_{f2}+L_{r2}\right)^2},\\
b_{21} &= b_{22} = -\frac{K_r(\alpha_r)m_r\left(L_{f2}+L_{r2}\right)-L_{rf}K_r(\alpha_r)\left(m_f+m_r\right)}{\left(m_f+m_r\right)\left(I_f+I_r+2m_r\left(L_{f2}+L_{r2}\right)^2\right)-m_r^2\left(L_{f2}+L_{r2}\right)^2},\\
b_{13} &= 0,\\
b_{23} &= \frac{1}{m_r^2 v_{xf}\left(L_{f2}+L_{r2}\right)^2-\left(m_f+m_r\right)v_{xf}\left(I_f+I_r+2m_r\left(L_{f2}+L_{r2}\right)^2\right)},\\
L_{\mathrm{rf}} &= L_{f2}+L_{r2}+L_{r1},\\
K_i(\alpha_i) &= \frac{C_{\alpha i}f(\xi_i)\tan\alpha_i}{\alpha_i\xi_i(1+\lambda_i)}.
\end{aligned}
\tag{12}
$$

3. Field Test and Model Validation

To validate the established lateral vehicle dynamic model and integrated simulation model built by MATLAB/Simulink and Recudyn, a field test is initiated. A speed sensor and IMU (inertial measurement unit) are mounted on the vehicle to detect the velocity and yaw rate during the test. The articulation angle is collected by a distance sensor, and based on the geometry transformation, the steering angle during the test can be acquired. A microcontrol unit, STM 32, is used to control the ASV. The layout of the sensors is demonstrated in Figure 3. The detail of the sensors is demonstrated in Table 1.

The steady steering maneuver is used during the field test, and the yaw rate and vehicle trajectory acquired during the test is compared to the value calculated by the established lateral dynamic model and integrated model (shown in Figures 4 and 5).

According to the demonstration in Figures 4 and 5, the calculated yaw rate and vehicle routine are in good correlation with the test result. In summary, the models could represent the dynamic characteristics accurately. Thus, the established models can be used in further analysis.

4. Integrated Controller Design

The gap between the ideal yaw rate and the actual yaw rate of the vehicle is a vital indicator to access vehicle stability [23]. The ideal yaw rate of the vehicle is determined by the vehicle speed and road adhesion coefficient. Normally, the vehicle's ideal yaw rate is acquired by the steady yaw rate gain. According to equation (11), the yaw rate gain of ASV can be gained.

$$\frac{\omega_i}{\theta}_s = \frac{v_x/L}{1 + K_s v_x^2}, \tag{13}$$

where K_s is the stability factor, which can be gained by the following equation:

$$K_s = \frac{\left(m_f + m_r\right)\left(L_{f1}K_f\left(\alpha_i\right) - L_{\mathrm{rf}}K_r\left(\alpha_i\right)\right) + m_r\left(L_{r2} + L_{f2}\right)\left(K_f\left(\alpha_i\right) + K_r\left(\alpha_i\right)\right)}{K_f\left(\alpha_i\right)K_r\left(\alpha_i\right)L^2}. \tag{14}$$

Since the lateral acceleration of the vehicle cannot exceed the maximum friction force between the tire and the road surface. When the vehicle is in a steady steering state, the boundary of lateral acceleration can be expressed as follows:

$$\omega_{i\max} v_{\mathrm{xf}} = \dot{v}_{vf} \le \mu g. \tag{15}$$

In summary, the idea yaw rate should meet the following equation:

$$\omega_{\mathrm{id}} = \min\left\{\left|\omega_i\right|, \left|\omega_{i\max}\right|\right\}\mathrm{sgn}\left(\theta\right). \tag{16}$$

According to equation (16), the yaw rate of the ASV varies with the articulation angle, and the road adhesion coefficient is illustrated in Figure 6.

As shown in Figure 6, the ideal yaw rate increases with the vehicle speed until the yaw rate reaches the boundary determined by the road adhesion coefficient. For example, when the vehicle runs on the road with a road adhesion coefficient of 0.2, the articulation angle is 2 degrees. The ideal yaw rate increases with the speed when the speed is in the range of 0 to 10 m/s and decreases with it when the speed is higher than 10 m/s.

Besides the yaw rate, the vehicle sideslip angle is another indicator of vehicle stability. According to the work of Eslamian et al. [24], based on equation (11), the steady vehicle sideslip angle during the constant cornering process is obtained as follows:

$$\frac{\beta_i}{\theta} = \frac{b_{21}a_{12} - b_{11}a_{22}}{a_{11}a_{22} - a_{12}a_{21}}. \tag{17}$$

The maximum sideslip angle is also related to the road adhesion coefficient, it can be defined by the following equation:

$$\left|\beta_{i\max}\right| \le \mathrm{atan}\left(0.02\mu g\right). \tag{18}$$

The vehicle sideslip angle corresponding to different articulation angles and road adhesion coefficient is shown in Figure 7.

As shown in Figure 7, the vehicle sideslip angle is inversely proportional to the articulation angle. Thus, the ideal vehicle sideslip angle can be expressed as follows:

$$\beta_{\mathrm{id}} = -\min\left\{\left|\beta_i\right|, \left|\beta_{i\max}\right|\right\}\mathrm{sgn}\left(\theta\right). \tag{19}$$

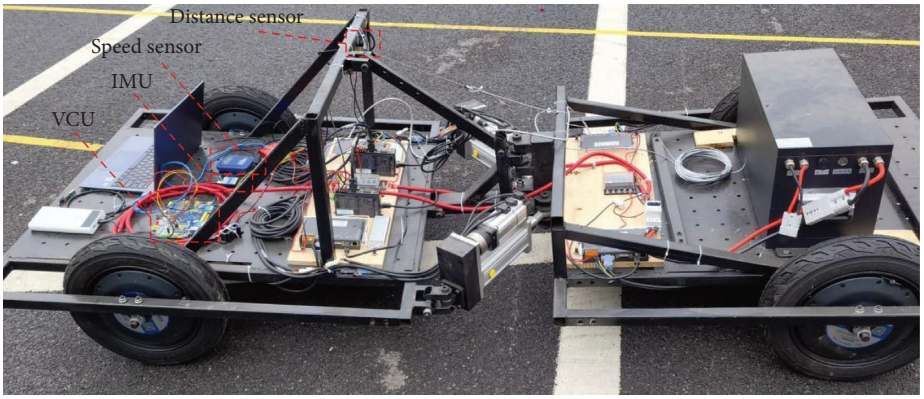

Figure 3: ASV with sensors.

Table 1: Detail of sensors.

Nos	Sensor	Type	Sampling frequency (Hz)
1	Distance sensor	BRT38-0.5M-COM1024-DC24	20
2	Speed sensor	V-box	10
3	IMU	HWT901-CAN	20
4	Vehicle control unit	STM 32	

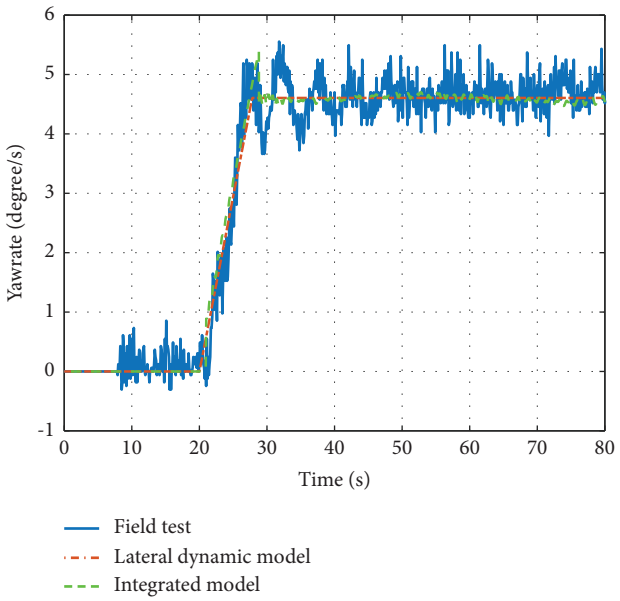

Figure 4: Comparison of yaw rate.

According to the illustration in Figure 7, the vehicle runs on the road with a lower road adhesion coefficient has a smaller region. To evaluate the vehicle stability, normally, the phase portrait, such as the $\beta - \omega$, $\beta - \dot{\beta}$, or tire sideslip phase portrait is chosen as the indicator. The $\beta - \dot{\beta}$ phase portrait is widely used in the stability assessment [12, 25–27]. Figure 8 shows the $\beta - \dot{\beta}$ phase portrait of the ASV. In Figure 8, the zone between the red dash lines is the stable area; otherwise, it is the unstable region.

The boundary of the stable region (the red dashed line in Figure 8) can be described by the following equation [28, 29]:

$$|a\dot{\beta} + b\beta| \leq 1. \tag{20}$$

The parameter a and b are acquired based on the stability boundary of the $\dot{\beta} - \beta$ phase portrait. When the vehicle is approaching the stability region, the vehicle will rush into an unstable state when the AFS system works. Thus, the control algorithm of AASS and DYC can be identified as Table 2.

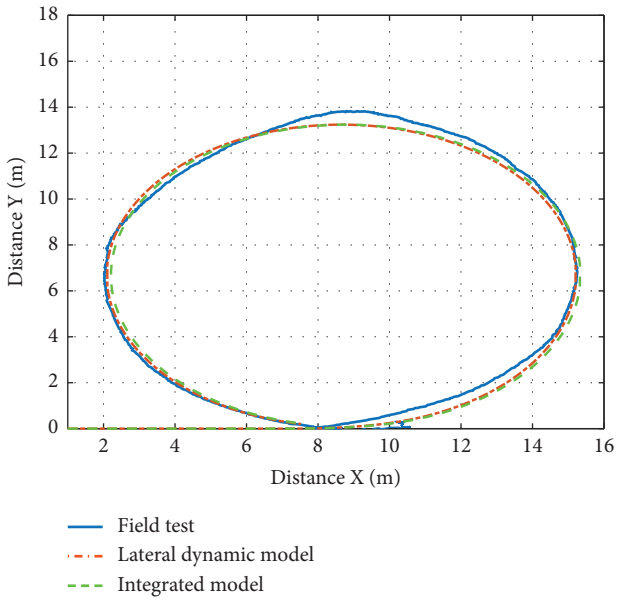

Figure 5: Comparison of vehicle trajectory.

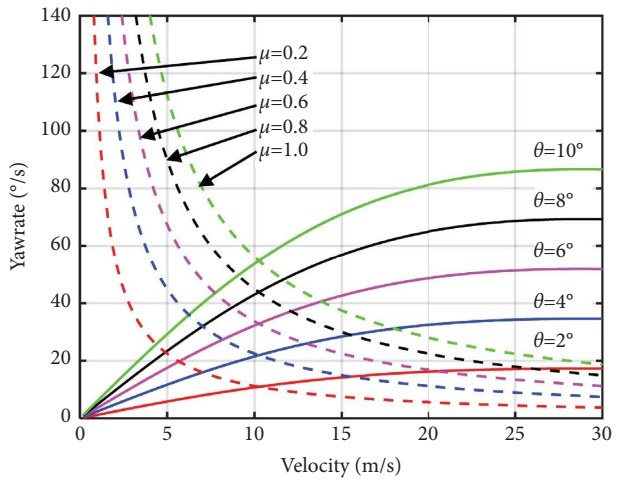

Figure 6: Ideal yaw rate of the ASV.

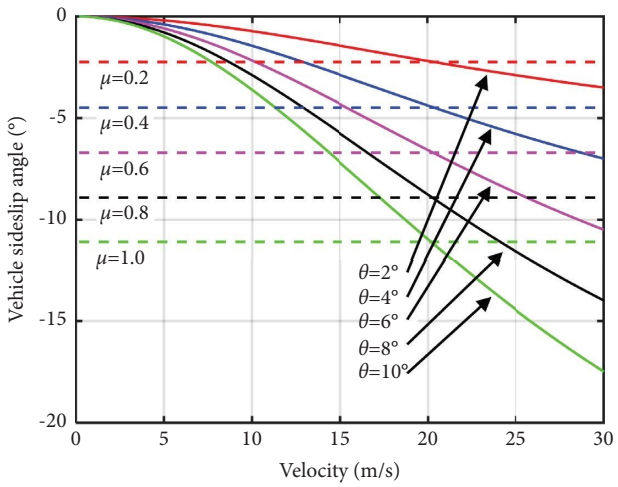

Figure 7: Ideal vehicle sideslip angle of the ASV.

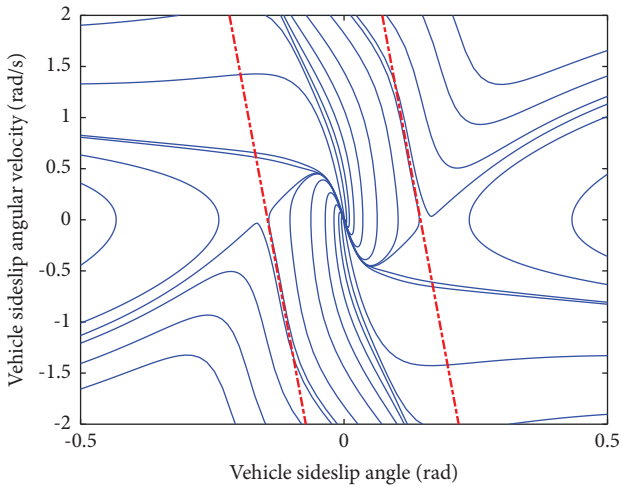

Figure 8: Phase portrait of the ASV.

Table 2: Control algorithm of AASS and DYC.

Stability criteria	Range	Functional system
$\lvert a\dot{\beta} + b\beta \rvert$	[0, 0.7]	AASS
	(0.7, 1]	AASS and DYC
	$(1, \infty)$	DYC

Normally, the ideal vehicle sideslip angle is set as zero [30, 31]. However, setting the vehicle sideslip angle as zero causes the DYC system initiated frequently. Based on equations (16) and (19), the ideal vehicle yaw rate and sideslip angle can be gained.

The state-space of the prediction model can be expressed as follows:

$$G_c\dot{X} = A_cX + B_cU + D_cW. \tag{21}$$

The state vector of the system X is defined as follows:

$$X = \left[\beta \;\; \omega \;\; F_{\text{yf}} \;\; F_{\text{yr}} \;\; e_{\omega\text{fl}} \;\; e_{\omega\text{fr}} \;\; e_{\omega\text{rl}} \;\; e_{\omega\text{rr}}\right]^T, \tag{22}$$

where F_{yf} and F_{yr} are the lateral force of the front and rear axle and $e_{\omega\text{ij}}$ is the error between the actual and ideal wheel speed. The input vector and disturbance vector of the system are

$$\begin{aligned} U &= \left[T_{\text{fl}} \;\; T_{\text{fr}} \;\; T_{\text{rl}} \;\; T_{\text{rr}}\right]^T, \\ W &= \left[a_x \;\; \widehat{F}_{\text{xfl}} \;\; \widehat{F}_{\text{xfr}} \;\; \widehat{F}_{\text{xrl}} \;\; \widehat{F}_{\text{xrr}}\right]^T, \end{aligned} \tag{23}$$

where T_{ij} and $\widehat{F}_{\text{xij}}$ are the torque and disturbance force of the motor and is the acceleration in the longitudinal direction.

The matrix to describable the system can be defined as follows:

$$A_c = \begin{bmatrix} -a_xm & -v_xm & \cos\theta & 1 & 0 & 0 & 0 & 0 \\ 0 & 0 & L_f\cos\theta & -L_r & 0 & 0 & 0 & 0 \\ 0 & 0 & 0 & 0 & k_{\text{fl}} & k_{\text{fr}} & 0 & 0 \\ 0 & 0 & 0 & 0 & 0 & 0 & k_{\text{rl}} & k_{\text{rr}} \\ 0 & 0 & 0 & 0 & 0 & 0 & 0 & 0 \\ 0 & 0 & 0 & 0 & 0 & 0 & 0 & 0 \\ 0 & 0 & 0 & 0 & 0 & 0 & 0 & 0 \\ 0 & 0 & 0 & 0 & 0 & 0 & 0 & 0 \end{bmatrix}, \tag{24}$$

where $m = m_f + m_r$, $L_f = L_{f1} + L_{f2}$, and $L_r = L_{r1} + L_{r2}$.

$$B_c = \begin{bmatrix} \frac{\sin\theta}{R_e} & \frac{\sin\theta}{R_e} & 0 & 0 \\ \frac{L_f \sin\theta - 0.5L_w\cos\theta}{R_e} & \frac{L_f \sin\theta + 0.5L_w\cos\theta}{R_e} & \frac{-L_w}{2R_e} & \frac{L_w}{2R_e} \\ 0 & 0 & 0 & 0 \\ 0 & 0 & 0 & 0 \\ -\frac{1}{I_w} & 0 & 0 & 0 \\ 0 & -\frac{1}{I_w} & 0 & 0 \\ 0 & 0 & -\frac{1}{I_w} & 0 \\ 0 & 0 & 0 & -\frac{1}{I_w} \end{bmatrix}, \tag{25}$$

$$D_c = \begin{bmatrix} 0 & 0 & 0 & 0 & 0 \\ 0 & 0 & 0 & 0 & 0 \\ 0 & 0 & 0 & 0 & 0 \\ 0 & 0 & 0 & 0 & 0 \\ \frac{1}{R_e} & \frac{R_e}{I_w} & 0 & 0 & 0 \\ \frac{1}{R_e} & 0 & \frac{R_e}{I_w} & 0 & 0 \\ \frac{1}{R_e} & 0 & 0 & \frac{R_e}{I_w} & 0 \\ \frac{1}{R_e} & 0 & 0 & 0 & \frac{R_e}{I_w} \end{bmatrix}, \tag{26}$$

$$G_c = \begin{bmatrix} v_x m & 0 & 0 & 0 & 0 & 0 & 0 & 0 \\ 0 & I_z & 0 & 0 & 0 & 0 & 0 & 0 \\ 0 & G_{32} & 1 & 0 & -\tilde{k}_{\mathrm{fl}} & -\tilde{k}_{\mathrm{fr}} & 0 & 0 \\ 0 & G_{42} & 0 & 1 & 0 & 0 & -\tilde{k}_{\mathrm{rl}} & -\tilde{k}_{\mathrm{rr}} \\ 0 & \frac{L_w}{2R_e} & 0 & 0 & 1 & 0 & 0 & 0 \\ 0 & -\frac{L_w}{2R_e} & 0 & 0 & 0 & 1 & 0 & 0 \\ 0 & \frac{L_w}{2R_e} & 0 & 0 & 0 & 0 & 1 & 0 \\ 0 & -\frac{L_w}{2R_e} & 0 & 0 & 0 & 0 & 0 & 1 \end{bmatrix}, \tag{27}$$

$$G_{32} = -\left(K_{\mathrm{yc,fl}}\widehat{A}_{\mathrm{fl}} + K_{\mathrm{yc,fr}}\widehat{A}_{\mathrm{fr}}\right), \tag{28}$$

$$G_{42} = -\left(K_{\mathrm{yc,rl}}\widehat{A}_{\mathrm{rl}} + K_{\mathrm{yc,rr}}\widehat{A}_{\mathrm{rr}}\right). \tag{29}$$

The state-space function of the discrete system can be gained based on the state-space formula of the continuous system.

$$\begin{cases} X_{k+1} = \mathrm{A}X_k + \mathrm{B}U_k + \mathrm{D}W_k, \\ Y_k = \mathrm{C}X_k, \end{cases} \tag{30}$$

where the footnotes k and $k+1$ are the state vectors at the step k and $k+1$. The output of the system, Y, is defined as follows:

$$Y = \left[\beta \;\; \omega \;\; e_{\omega\mathrm{fl}} \;\; e_{\omega\mathrm{fr}} \;\; e_{\omega\mathrm{rl}} \;\; e_{\omega\mathrm{rr}}\right]^T. \tag{31}$$

The system matrix can be gained based on equations (24)~(27).

$$\begin{aligned} A &= I + G_c^{-1}A_c\Delta T, \\ B &= G_c^{-1}B_c\Delta T, \\ D &= G_c^{-1}D_c\Delta T, \end{aligned} \tag{32}$$

where I is a unit matrix and ΔT means the time step.

The steering angle θ and vehicle speed v_x are assumed as constant during the k to $k+1$ step. Thus, the optimal solution of the model prediction control can be gained.

$$\begin{cases} J = \dfrac{1}{2}\displaystyle\sum_{k=1}^{N_p}\left(\left\|Y^k - Y_d^k\right\|_Q^2 + \left\|U^k - U^d\right\|_R^2 + \left\|U^k - U^{k-1}\right\|_T^2\right), \\ \overline{U}^* = \mathrm{argmin}\,(J), \end{cases} \tag{33}$$

where N_p means the predicted time step, Y_d is the ideal state, U^d is the torque distribution of the driving wheels. Q, R, and T are the weight matrix. $\overline{U}^*$ is the predicted output sequence that meets the minimum objective J.

$$\begin{aligned} Y_d &= \left[\beta_d \;\; \omega_d \;\; 0 \;\; 0 \;\; 0 \;\; 0\right]^T, \\ U_d &= T_c\left[\frac{F_{\mathrm{zf}}}{2\left(F_{\mathrm{zf}}+F_{\mathrm{zr}}\right)} \;\; \frac{F_{\mathrm{zf}}}{2\left(F_{\mathrm{zf}}+F_{\mathrm{zr}}\right)} \;\; \frac{F_{\mathrm{zr}}}{2\left(F_{\mathrm{zf}}+F_{\mathrm{zr}}\right)} \;\; \frac{F_{\mathrm{zr}}}{2\left(F_{\mathrm{zf}}+F_{\mathrm{zr}}\right)}\right]^T. \end{aligned} \tag{34}$$

According to the QP (quadratic problem) method and constraint of the motor and tire, $\overline{U}_d$ can be gained and taken as the output of the MPC controller.

Two independent input is needed to track two system status (β_d, ω_d). There are two inputs in this system, but they are not independent. The importance of the system status is determined by the weight coefficient, q_1 and q_2, in the matrix Q. Normally, the yaw rate focuses on the vehicle handling performance while the vehicle sideslip angle focuses on the stability. When the vehicle is in a stable region, better handling performance is expected. When the vehicle is in an unstable region, stability performance is more important. Thus, to improve the performance of the controller, the weight coefficient, q_1 and q_2, is determined by the stability criteria. Therefore, this MPC controller is adaptive to the vehicle stability criteria.

5. Discussion

For the assessment of the vehicle's lateral stability, there are some classic maneuvers, such as steady steering, snake steering, fishhook, double lane-change, and 0.7 sine with dwell maneuver. Among them, the double lane-change and fishhook are the most common conditions in the relevant research. They are chosen to compare the lateral stability performance with the provided control algorithm and an antiwindup PID controller proposed in the paper [32]. The double lane-change is initiated based on the regulation in ISO-3888-1-2018 (passenger cars-test track for a severe lane-change maneuver: obstacle avoidance), and 0.7 sine with dwell maneuver is regulated in Federal Motor Vehicle Safety Standard (FMVSS) No. 126, Electronic Stability Control (ESC) System.

An HIL (hardware in loop) platform is used to verify the lateral stability control algorithm. As shown in Figure 9, the platform is made up of three parts, data visualization system, dSPACE Micro AutoBox, and SCALEXiO. The data visualization system displays the data from the Micro Auto Box and SCALEXiO and input the driver's intention. The reference model, state estimator, and stability assessment and control algorithm is integrated in the Micro AutoBox. It acts as the VCU (vehicle control unit) in a practical vehicle. The vehicle dynamic model, motor controller model, road model is set in the SCALEXiO.

5.1. Double Lane-Change. The vehicle should shift from the original to the paralleled one and back to the original one without hitting the barriers during the double lane-change. The barriers are regulated in ISO-3888-1-2018. The vehicle

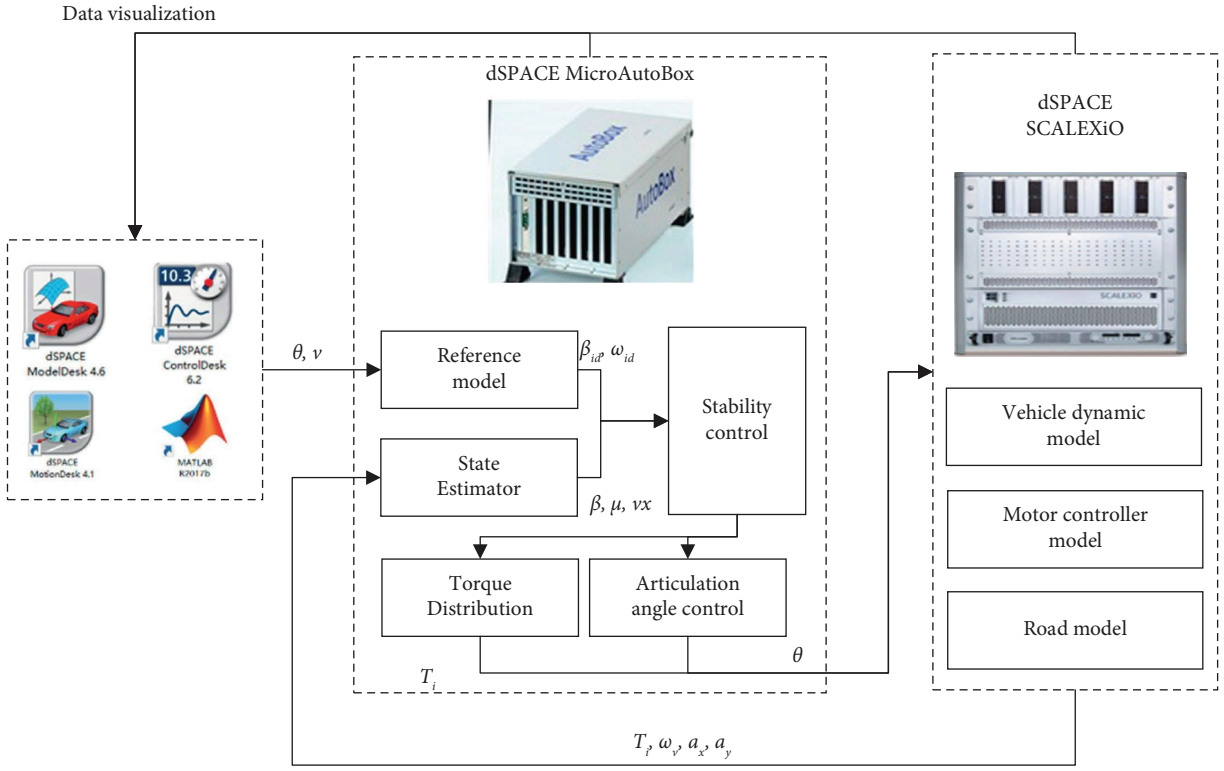

Figure 9: HIL platform.

yaw rate and sideslip angle of the reference model, without control method, with the provided adaptive MPC controller and antiwindup PID controller, are compared in Figures 9 and 10. The output of the reference model is taken as the baseline.

In Figures 10 and 11, with the provided adaptive MPC controller, the yaw rate and vehicle sideslip angle have the minimum error. Without the controller, the yaw rate and vehicle sideslip have the maximum gap from the baseline. The performance of the antiwindup PID controller is between the provided controller and without any control.

The vehicle trajectory is illustrated in Figure 12. Without control, the vehicle fails to pass the maneuver for contacting the upper boundary. With the adaptive MPC and antiwindup PID controller, the vehicle can pass the test. The minimum trajectory error occurs in the vehicle with an adaptive MPC controller.

5.2. 0.7 Sine with Dwell Maneuver. The steering input of the 0.7 sine with dwell maneuver is illustrated in Figure 13. It is widely used in this area due to its objectivity, practicability, repeatability, and representativeness.

In this test, the two lateral criteria are defined as the ratio of the vehicle yaw rate at a specified time to the first local peak yaw rate generated by 0.7 Hz sine with dwell steering reversal. They can be represented in the mathematical notations as follows:

$$L_{c1} = \frac{\omega_{(t_0+1)}}{\omega_{\text{peak}}} \times 100 \leq 35\%, \tag{35}$$

$$L_{c2} = \frac{\omega_{(t_0+1.75)}}{\omega_{\text{peak}}} \times 100 \leq 20\%, \tag{36}$$

where ω_t means the yaw rate at the time t, ω_{peak} is the first local peak yaw rate generated by the 0.7 Hz sine with dwell steering input, and t_0 represents the time to completion of steering input.

Figure 14 shows the yaw rate of the four models. The absolute value of the reference peak yaw rate is lower than the other three models. Without control, the model has the maximum peak value. The yaw rate in equations (35) and (36) can be extracted from Figure 14 and is shown in Table 3.

According to equations (35) and (36), all of three models meet the lateral criteria. Because of the low ω_{peak} value, the L_{c1} and L_{c2} of the adaptive MPC controller is higher than the PID controller. The criteria of the model with PID controller have the minimum criteria, which means it has the fastest yaw rate decrease rate. With the adaptive MPC controller, the model has the minimum peak value but the lowest decrease rate. The variation of vehicle sideslip angle is compared in Figure 15.

As shown in the comparison, the peak value of the sideslip angle of the three models is higher than the reference model. Taking the reference model as the baseline, the model without control has the maximum deviation value, and the model with adaptive MPC has the minimum deviation value. All of the peak values of the three models fluctuate, and the fluctuation range gets smaller.

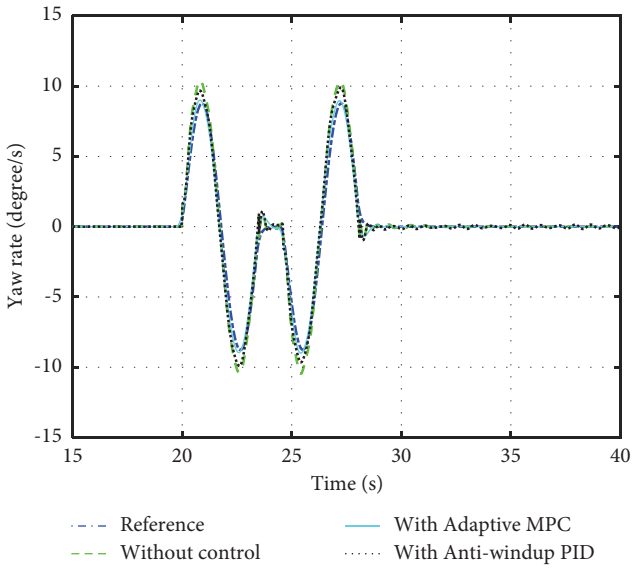

Figure 10: Comparison of yaw rate.

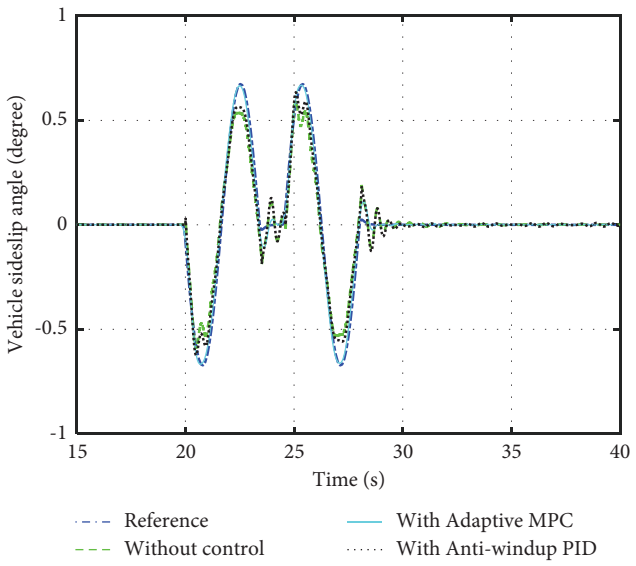

Figure 11: Comparison of vehicle sideslip angle.

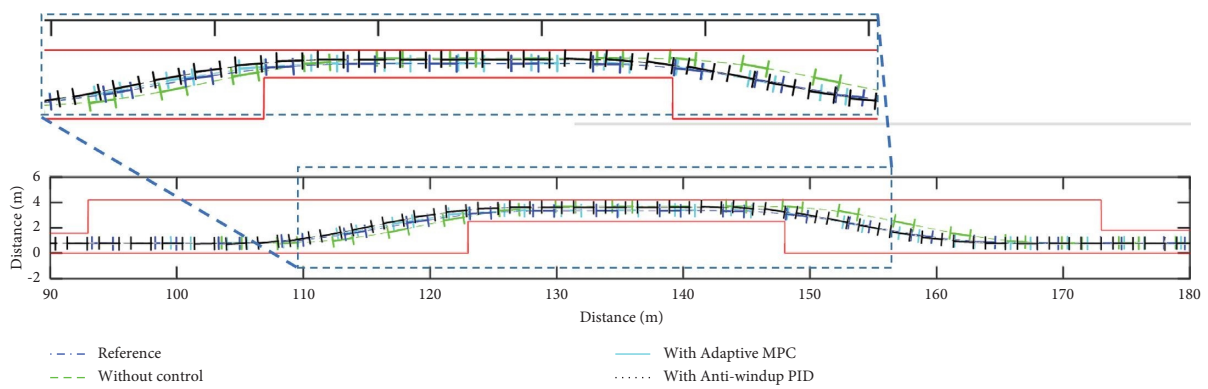

Figure 12: Comparison of vehicle trajectory.

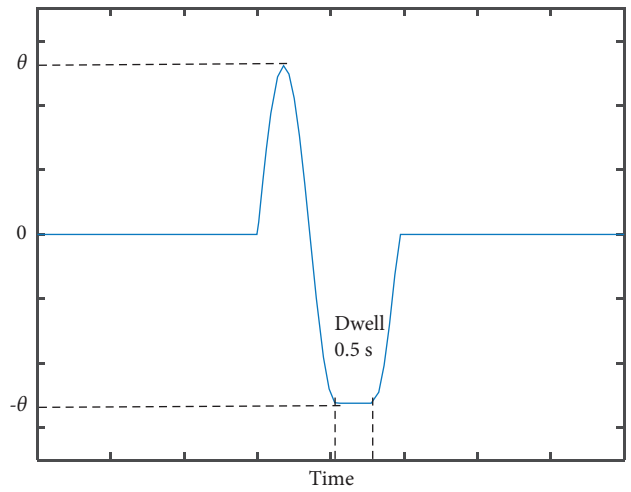

Figure 13: Steering angle input of 0.7 Hz sine with dwell maneuver.

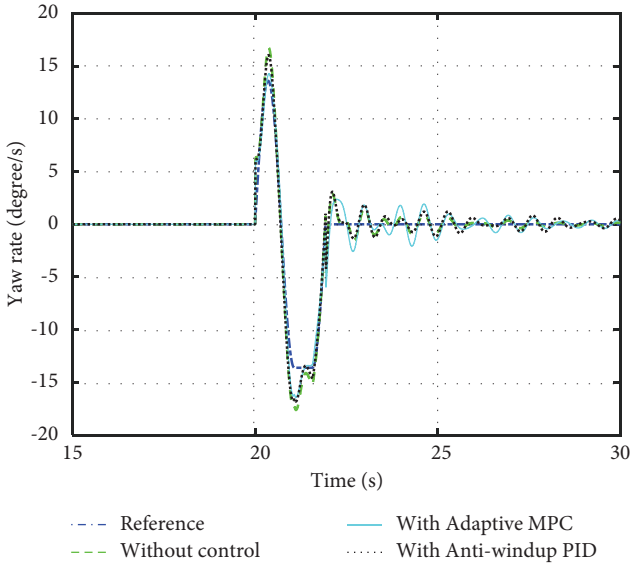

Figure 14: Comparison of yaw rate.

Table 3: Yaw rate value during the 0.7 Hz sine with dwell maneuver.

Models	Reference	Without control	With MPC	With PID
ω_{peak}	13.65	16.67	14.27	16.01
$\omega_{(t_0+1)}$	0	3.69	2.55	2.78
$\omega_{(t_0+1.75)}$	0	1.19	2.05	0.83
L_{c1}	0	22.14	17.87	17.36
L_{c2}	0	7.14	14.37	5.18

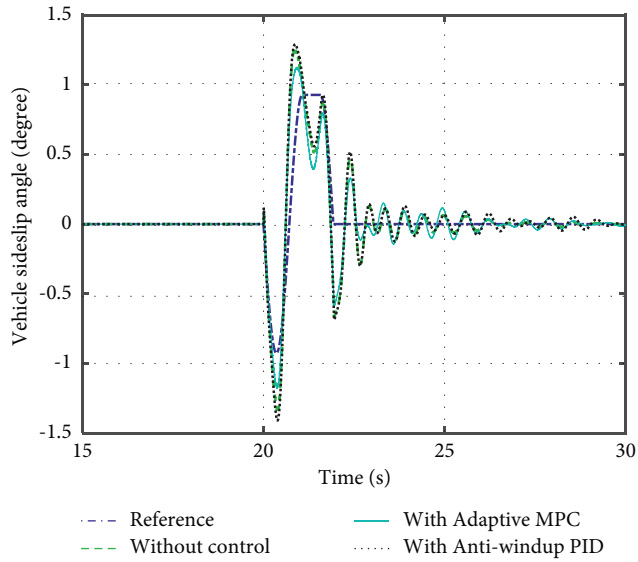

Figure 15: Comparison of vehicle sideslip angle.

6. Conclusion

The ASV is widely used in the special and engineering vehicle area due to its unique characteristics. It also has the disadvantage of weak lateral stability. To deal with its shortcoming, the lateral dynamic model of the ASV is established based on the dynamic theory. The built model is validated by the field test result. The state-space formula of the ASV is more complicated than the vehicle with an Ackerman steering system. The corresponding ideal yaw rate and vehicle sideslip angle expression also differ from the regular car, especially for the ideal vehicle sideslip angle. For the ASV, the ideal vehicle sideslip angle and articulated angle have the opposite sign; however, for the regular vehicle, the sideslip angle and steering angle have the same sign.

According to the lateral stability analysis, an integrated AAFS and DYC based on MPC theory is provided based on the vehicle sideslip angle and sideslip angular velocity phase portrait. The vehicle performance with the provided adaptive MPC controller and antiwindup PID controller during two typical lateral stability tests is compared. According to the comparison, in the double lane-change test, the vehicle with MPC and PID controller can help the vehicle to pass the test, the vehicle with MPC has a more ideal routine. In the 0.7 Hz sine with dwell maneuver test, the vehicle with MPC has the minimum peak value and deviation value after the steering process, and the vehicle with PID control has the maximum recovery rate.

With the provided integrated controller, the lateral stability of the ASV is improved. Hence, the vehicle safety and path-tracking ability are strengthened, which will benefit the construction of the ITS with the ASV.

Abbreviations

m_f: Front vehicle body mass
m_r: Rear vehicle body mass
v_{yf}: Front vehicle body lateral velocity
v_{yr}: Rear vehicle body lateral velocity
F_{yfl}: Lateral force of front left tire
F_{yrl}: Lateral force of rear left tire
F_{yfr}: Lateral force of front right tire
F_{yrr}: Lateral force of rear right tire
I_f: Front vehicle body yaw moment of the inertia
I_r: Rear vehicle body yaw moment of the inertia
L_{f1}: Distance between the front axle and CG of front vehicle body
L_{f2}: Distance between the articulation point and CG of front vehicle body
L_{r1}: Distance between the rear axle and CG of rear vehicle body
L_{r2}: Distance between the articulation point and CG of rear vehicle body
ω: Vehicle yaw rate
β: Vehicle sideslip angle
C_{xi}: Longitudinal stiffness of the tire
$C_{\alpha i}$: Lateral stiffness of the tire
λ_i: Slip rate of wheel
μ: Road adhesion coefficient
α_i: Side slip angle of tire
θ: Articulation angle
F_{zf}: Front axle load
F_{zf}: Rear axle load
α_{sl}: Sideslip angle that corresponds to the full saturation of the lateral tire force
$x(t)$: State vector of state-space
A: System matrix
B_1: Control input matrix for control vector 1
B_2: Control input matrix for control vector 2
$u_1(t)$: Control vector 1
$u_2(t)$: Control vector 2
ω_i: Ideal yaw rate
K_s: Stability factor
$\omega_{i\max}$: Maximum ideal yaw rate
ω_{id}: Desired ideal yaw rate

β_i: Ideal vehicle sideslip angle
$\beta_{i\max}$: Maximum ideal vehicle sideslip angle
β_{id}: Desired ideal vehicle sideslip angle
a: Fitted parameter for stability boundary function
b: Fitted parameter for stability boundary function
X: State vector of the prediction model state-space
$e_{\omega\mathrm{ij}}$: Error between the actual and ideal wheel speed
U: Input vector of the prediction model state-space
W: Disturbance vector of the prediction model state-space
A_c: System matrix of the prediction model state-space
W: Control matrix of the prediction model state-space
T_{ij}: Motor torque
$\widehat{F}_{\mathrm{xij}}$: Motor disturbance force
$\overline{U}^*$: Predicted output sequence that meets the minimum objective
$\overline{U}_d$: First sequence of the predicted output sequence.

Data Availability

The data used to support the findings of this study are available from the corresponding author upon request.

Conflicts of Interest

The authors declare that there are no conflicts of interest.

Acknowledgments

This study was funded by the Innovative Research Team Development Program of Ministry of Education of China (Grant no. IRT_17R83) and the 111 Project (Grant no. B17034) of China.

References

[1] B. J. Alshaer, T. T. Darabseh, and A. Q. Momani, "Modelling and control of an autonomous articulated mining vehicle navigating a predefined path," *International Journal of Heavy Vehicle Systems*, vol. 21, pp. 152–168, 2014.

[2] G. Bai, L. Liu, Y. Meng, W. Luo, Q. Gu, and B. Ma, "Path tracking of mining vehicles based on nonlinear model predictive control," *Applied Sciences*, vol. 9, p. 1372, 2019.

[3] X. Jin, G. Yin, C. Bian, J. Chen, P. Li, and N. Chen, "Gain-scheduled vehicle handling stability control via integration of active front steering and suspension systems," *Journal of Dynamic Systems, Measurement, and Control*, vol. 138, Article ID 014501, 2016.

[4] Z. Wang, X. Ding, and L. Zhang, "Chassis coordinated control for full x-by-wire four-wheel-independent-drive electric vehicles," *IEEE Transactions on Vehicular Technology*, vol. 72, no. 4, 2022.

[5] N. Aouadj, K. Hartani, and M. Fatiha, "New integrated vehicle dynamics control system based on the coordination of active front steering, direct yaw control, and electric differential for improvements in vehicle handling and stability," *SAE International Journal of Vehicle Dynamics, Stability, and NVH*, vol. 4, no. 2, pp. 119–133, 2020.

[6] X. Jin, Z. Yu, and G. Yin, "Improving vehicle handling stability based on combined AFS and DYC system via robust Takagi-Sugeno fuzzy control," *IEEE Transactions on Intelligent Transportation Systems*, vol. 19, no. 8, pp. 2696–2707, 2017.

[7] Y. Zhang, A. Khajepour, E. Hashemi, Y. Qin, and Y. Huang, "Reconfigurable model predictive control for articulated vehicle stability with experimental validation," *IEEE Transactions on Transportation Electrification*, vol. 6, no. 1, pp. 308–317, 2020.

[8] A. Tahouni, M. Mirzaei, and B. Najjari, "Novel constrained nonlinear control of vehicle dynamics using integrated active torque vectoring and electronic stability control," *IEEE Transactions on Vehicular Technology*, vol. 68, no. 10, pp. 9564–9572, 2019.

[9] C. Wang, Z. Wang, L. Zhang, H. Yu, and D. Cao, "Post-impact motion planning and tracking control for autonomous vehicles," *Chinese Journal of Mechanical Engineering*, vol. 35, no. 1, p. 54, 2022.

[10] L. Zhang, Z. Wang, X. Ding, S. Li, and Z. Wang, "Fault-tolerant control for intelligent electrified vehicles against front wheel steering angle sensor faults during trajectory tracking," *IEEE Access*, vol. 9, pp. 65174–65186, 2021.

[11] X. Ding, Z. Wang, and L. Zhang, "Hybrid control-based acceleration slip regulation for four-wheel-independent-actuated electric vehicles," *IEEE Transactions on Transportation Electrification*, vol. 7, no. 3, pp. 1976–1989, 2021.

[12] H. Zheng, L. Wang, and J. Zhang, "Comparison of active front wheel steering and differential braking for yaw/roll stability enhancement of a coach," *SAE International Journal of Vehicle Dynamics, Stability, and NVH*, vol. 2, no. 4, pp. 267–283, 2018.

[13] D. Peng, K. Fang, J. Kuang, M. A. Hassan, and G. Tan, "Conflict and sensitivity analysis of articulated vehicle lateral stability based on single-track model," *Shock and Vibration*, vol. 2021, Article ID 5893993, 18 pages, 2021.

[14] A. Rehnberg, L. Drugge, and A. S. Trigell, "Snaking stability of articulated frame steer vehicles with axle suspension," *International Journal of Heavy Vehicle Systems*, vol. 17, no. 2, pp. 119–138, 2010.

[15] X. Zhang, Q. Liu, J. Liu, Q. Zhu, and H. Hu, "Using gyro stabilizer for active anti-rollover control of articulated wheeled loader vehicles," vol. 235, no. 2, pp. 237–248, 2021.

[16] M. Kumar, A. C. Hildebrandt, P. Strauss, S. Kraus, C. Stiller, and A. Zimmermann, "Lateral trajectory stabilization of an articulated truck during reverse driving maneuvers," in *Proceedings of the 4th 2020 IEEE Intelligent Vehicles Symposium*, IEEE, Las Vegas, NV, USA, November 2020.

[17] Y. Gao, Y. Shen, T. Xu, W. Zhang, and L. Güvenç, "Oscillatory yaw motion control for hydraulic power steering articulated vehicles considering the influence of varying bulk modulus," *IEEE Transactions on Control Systems Technology*, vol. 27, no. 3, pp. 1284–1292, 2019.

[18] L. Gao, F. Ma, and C. Jin, "A model-based method for estimating the attitude of underground articulated vehicles," *Sensors*, vol. 19, no. 23, p. 5245, 2019.

[19] R. He and H. Yun, "Electronic differential control of the rear-wheel independent-drive electric vehicle," *SAE International Journal of Vehicle Dynamics, Stability, and NVH*, vol. 4, pp. 49–65, 2019.

[20] A. Tahouni, M. Mirzaei, and B. Najjari, "Applied nonlinear control of vehicle stability with control and state constraints," *Part D: Journal of Automobile Engineering*, vol. 234, no. 1, pp. 191–211, 2020.

[21] N. Borchardt, R. Kasper, and W. Heinemann, "Design of a wheel-hub motor with air gap winding and simultaneous

utilization of all magnetic poles," in *Proceedings of the 2012 IEEE International Electric Vehicle Conference*, IEEE, Greenville, SC, USA, March 2012.

[22] Pacejka and B. Hans, *Tire and Vehicle Dynamics*, Science Direct, Amsterdam, The Netherlands, 3rd edition, 2012.

[23] C. Geng, L. Mostefai, M. Denaï, and Y. Hori, "Direct yaw-moment control of an in-wheel-motored electric vehicle based on body slip angle fuzzy observer," *IEEE Transactions on Industrial Electronics*, vol. 56, no. 5, pp. 1411–1419, 2009.

[24] M. Eslamian, G. Alizadeh, and M. Mirzaei, "Optimization-based non-linear yaw moment control law for stabilizing vehicle lateral dynamics," *Part D: Journal of Automobile Engineering*, vol. 221, no. 12, pp. 1513–1523, 2007.

[25] S. M. M. Jaafari and K. Heidari Shirazi, "A comparison on optimal torque vectoring strategies in overall performance enhancement of a passenger car," *Part K: Journal of Multi-body Dynamics*, vol. 230, no. 4, pp. 469–488, 2016.

[26] L. Guo, P. Ge, and D. Sun, "Torque distribution algorithm for stability control of electric vehicle driven by four in-wheel motors under emergency conditions," *IEEE Access*, vol. 7, pp. 104737–104748, 2019.

[27] J. Zhu, S. Zhang, G. Wang, W. Zhang, and S. Zhang, "Research on vehicle stability region under critical driving situations with static bifurcation theory," *Part D: Journal of Automobile Engineering*, vol. 235, no. 8, pp. 2072–2085, 2021.

[28] J. He, D. A. Crolla, M. C. Levesley, and W. J. Manning, "Coordination of active steering, driveline, and braking for integrated vehicle dynamics control," *Part D: Journal of Automobile Engineering*, vol. 220, no. 10, pp. 1401–1420, 2006.

[29] Y. Wang, Y. Lei, and P. Wang, "Integrated stability control for a vehicle in the vehicle-to-grid system on low adhesion coefficient road," *Frontiers in Energy Research*, vol. 10, pp. 1–11, 2022.

[30] H. Zhang, X. Zhang, and J. Wang, "Robust gain-scheduling energy-to-peak control of vehicle lateral dynamics stabilisation," *Vehicle System Dynamics*, vol. 52, no. 3, pp. 309–340, 2014.

[31] H. Zhang and J. Wang, "Vehicle lateral dynamics control through AFS/DYC and robust gain-scheduling approach," *IEEE Transactions on Vehicular Technology*, vol. 65, no. 1, pp. 489–494, 2016.

[32] E. D. Puchta, R. Lucas, F. R. Ferreira, H. V. Siqueira, and M. S. Kaster, "Gaussian adaptive PID control optimized via genetic algorithm applied to a step-down DC-DC converter," in *Proceedings of the 2016 12th IEEE International Conference on Industry Applications (INDUSCON)*, IEEE, Curitiba, Brazil, November 2016.